RSC Advances

ROYAL SOCIETY OF CHEMISTRY

www.rsc.org/advances

Enhanced Photovoltaic Performance of Inverted Polymer Solar Cells by Incorporating Graphene Nanosheet/AgNPs Nanohybrids

Yu-An Su[1], Wei-Chen Lin[2], Hsing-Ju Wang[1], Wan-Hua Lee[2], Rong-Ho Lee[2]*, Shenghong A. Dai[2], Chi-Fa Hsieh[3], and Ru-Jong Jeng[1]*

[1] Institute of Polymer Science and Engineering, National Taiwan University, Taipei 106, Taiwan

[2] Department of Chemical Engineering, National Chung Hsing University, Taichung 402, Taiwan

[3] Chung-Shan Institute of Technology, Lungtan, Taoyuan 325, Taiwan

*Corresponding authors. RHL, Tel.: +886-4-2285-4308; Fax: +886-4-2285-4734; RJJ, Tel.: +886-2-3366-5884; Fax: +886-2-3366-5237

E-mail: rhl@nchu.edu.tw (RHL), rujong@ntu.edu.tw (RJJ)

ABSTRACT

A linear-dendritic block copolymer (LDBC) functionalized exfoliated graphene nanosheets (XGS)/silver nanoparticles (AgNPs) was prepared for using as the interfacial layer between the zinc oxide (ZnO) based electron-selective layer and poly(3-hexylthiophene) (P3HT)/fullerene derivative ($PC_{61}BM$) blend based photoactive layer in an inverted polymer solar cell (PSC). The LDBCs were prepared by the respective addition reaction of a hydrophilic poly(oxyalkylene)amine with hydrophobic dendrons of various generations based on 4-isocyanate-4′-(3,3-dimethyl-2,4-dioxo-azetidine)-diphenylmethane (IDD). The dendrons having polyurea/malonamide functionalities were synthesized by using IDD as a building block. Moreover, the dendrons comprised not only hydrogen bond-rich malonamide linkages, but long alkyl chains at the peripheries as well. XGS were respectively grafted with these amphiphilic LDBCs to afford XGS-dendritic derivatives (XGS-G0.5, XGS-G1.5, and XGS-G2.5). Subsequently, a nanohybrid, XGS-G2.5/AgNPs was obtained through the reduction of Ag^+ on the surface of LDBC modified XGS. The dendrons would serve as the effective templates for hosting AgNPs. By the incorporation of XGS-G2.5/AgNPs nanohybrid, it rendered the PSC an increased power conversion efficient (PCE) to 4.04 %, a 19.5 % improvement over a PCE of 3.38 % for the bare inverted PSC, due to the localized surface plasmon resonance of AgNPs, and the improvement of compatibility and charge transfer capacity between ZnO based cathode and photoactive layer.

Keywords: exfoliated graphene sheet, silver nanoparticle, polymer solar cell.

1. Introduction

Bulk heterojunction (BHJ) solar cells based on low-band gap π-conjugated polymers have received much attention because of their great potential for the development of solution-processable, highly flexible, large-area, low cost, light-weight solar modules [1-2]. The photoactive layer in a typical BHJ cell is based on a blend of a conjugated polymer as the electron donor and a high-electron-affinity fullerene derivative as the electron acceptor [3-5]. The photovoltaic (PV) performance of polymer solar cells (PSCs) has improved significantly in the past decade through the optimization of the device structure, interfacial layer engineering, and processing conditions [6-12]. Nevertheless, PSCs with the conventional structures suffer from device degradation due to the diffusion of oxygen into the active layer through the pinholes of the metal cathode, and the corrosion of ITO by the hole-transporting layer of acidic PEDOT:PSS [13-14]. Therefore, using an ITO coated substrate as a cathode and a high work function metal as the top anode in inverted structural PSCs has been considered as an advantageous approach to improve cell stability [15-18].

In order to reduce the electron extraction barrier and enhance the electron-extraction efficiency, an additional interfacial or electron-selective layer is usually inserted between the ITO cathode and photoactive layer [19-41]. Metal oxides, such as zinc oxide (ZnO) and titanium oxide (TiO_2), with high electron-mobility, efficient electron-extraction, and good hole-blocking capacity, have been widely used as the cathode interfacial layer [19-22]. Although the operational stability under air has been improved for the inverted PSCs, these cells still suffer from the inherent incompatibility and poor electrical contact at the interface between the inorganic metal oxides and polymer based photoactive layer [23]. In order to further lower the energy barrier for electron-transport and reduce the inherent incompatibility between the metal oxide and conjugated polymer based photoactive layer, the water soluble polymer electrolytes or conjugated polymer electrolytes have been coated on the top of metal oxide layer or blended with the metal oxide, and used as the electron-selective layer of inverted PSCs [24-31]. The non-conjugated polyethyleneimine (PEI) has been successfully employed for

forming the interfacial layer on ITO for the inverted PSCs. The PEI can lower the work function of an ITO cathode and facilitate the collection of photogenerated charge carrier by forming interfacial dipoles [24, 25]. In addition, the PV performance of inverted PSCs could be enhanced by tuning the surface energy of ZnO layer with a self-assembled monolayer (SAM) composed of the aminesilane and alkylsilane components [32]. Apart from that, ionic liquid modified carbon materials and acid functionalized fullerene derivatives based SAMs have been studied for using as the electron-selective layer of inverted PSCs [33-39]. The use of interfacial SAMs was found to be efficient in facilitating charge transfer between the metal oxides and photoactive layer, resulting in an improved PV performance by reducing the contact resistance and passivating the inorganic surface trap sites [35-39]. Moreover, the incorporation of electro-active SAMs indicates that the SAMs may provide an additional pathway for photo-induced charge transfer and charge collection from photoactive layer to ITO cathode [37]. On the other hand, the graphene materials with unique photonic and electric properties have been used as the material of electron-selective layer or blended into the metal oxide based buffer layer in the inverted PSCs [40]. The use of graphene nanosheets as an interfacial layer would enhance the PV performance of inverted PSCs due to the enhancement of exciton dissociation and the suppression of free charge recombination at the cathode/photoactive layer interface [40]. Lee et al. reported that the blend of the reduced graphene oxide (RGO) into the ZnO based electron-selective layer would enhance the electron conductivity, and reduced the contact resistance at the ZnO/photoactive layer interface [41]. Consequently, better PV performance was observed for the inverted PSCs. Zhang et al. reported that the presence of the TiO_2/RGO based interfacial layer would enhance the electron collecting efficiency, and resulted in a large open circuit voltage (V_{OC}) of inverted PSC [42]. In addition, cesium carbonate functionalized graphene nanosheets have been inserted between the ITO and photoactive layer as the interface for the improvement of the electron-extraction, and the suppression of leakage current of inverted PSCs. As a result, a higher power conversion efficiency (PCE) and better operational stability were achieved for PSCs [43]. Apart from that, the inclusion of metal nanoparticles (NPs) in the electron-transporting or hole-transporting interfacial layer of inverted PSCs has received much attention

for enhancing PV performance [44-45]. Xie et al. reported that the photocurrent density and efficiency of inverted PSC were enhanced significantly as the silver or gold nanoparticles (AgNPs or AuNPs) were embedded in the TiO_2 based electron-selective layer [44]. The charge extraction enhancement under solar illumination can be explained by the transfer of UV-excited electrons from the TiO_2 electron-transport layer to metal NPs, and the enhanced accumulation of the electrons in TiO_2-NPs composites. The electron accumulation would reduce the work function of the electron-transport composite. The re-distribution of charges in the UV-irradiated TiO_2-NPs system can assist the charge extraction in PSCs. Moreover, Li et al. reported that the addition of AgNPs in a molybdenum oxide (MoO_x) based hole-transporting layer would enhance the PV performance of inverted PSC due to the improvement of the electrical properties of the MoO_x layer [45]. Apart from that, Shahjamali et al. showed that plasmonic gold coated AgNPs (GSNPs) act as optical antennae to substantially enhance light absorption in the photo-active layer of PSC when GSNPs were embedded in the device [46].

In this study, a series of linear-dendritic block copolymer (LDBC) functionalized exfoliated graphene nanosheets (XGS) were prepared for using as the interfacial layer between the ZnO based electron-transporting layer and poly(3-hexylthiophene) (P3HT)/fullerene derivative ($PC_{61}BM$) blend based photoactive layer in an inverted PSC. The XGS were prepared from the exfoliation of graphite oxide (GO) in an acidic environment [47]. Moreover, the LDBCs were synthesized by the addition reactions of a hydrophilic poly(oxyalkylene)amine with hydrophobic dendrons of various generations based on 4-isocyanate-4′-(3,3-dimethyl-2,4-dioxo-azetidine)-diphenylmethane (IDD). The dendrons having polyurea/malonamide functionalities were synthesized by using IDD as a building block [48, 49]. Moreover, the dendrons comprised hydrogen bond-rich malonamide linkages and long alkyl chains at the peripheries. The co-presence of hydrogen bonding interactions and large contents of hydrophobic moieties allowed the dendrons to serve as surfactants for the modification of graphene nanosheets [50, 51]. XGS were grafted with such amphiphilic LDBCs to afford XGS-dendritic derivative nanohybrids (XGS-G0.5, XGS-G1.5, and XGS-G2.5). Furthermore, a new XGS-G2.5/AgNPs nanohybrid was prepared through the reduction of Ag^+ on the surface of dendron modified XGS (XGS-G2.5). The 2.5

generation dendrons with high degree of branching could serve as the effective templates for hosting AgNPs [52]. This led to better dispersion of AgNPs in XGS-G2.5, i.e. XGS functionalized with higher generation of dendron [53]. As a result, the electrical conductivity between graphene nanosheets was enhanced by the incorporation of AgNPs [54]. Moreover, it has been reported that the graphene/AgNPs composites were incorporated into the photoactive layer of PSC to enhance the PV performance [55]. Nevertheless, the graphene nanosheets/AgNPs nanohybrid has not been studied for using as the interfacial layer in inverted PSCs. In order to improve the dispersity of XGS-G2.5 and XGS-G2.5/AgNPs nanohybrids on the surface of ZnO layer, the XGS-G2.5 and XGS-G2.5/AgNPs nanohybrids were respectively dispersed into the PEI solutions and spin-coated on the ZnO layers. By inserting the PEI/XGS-G2.5 or PEI/XGS-G2.5/AgNPs as the interfacial layer, the PV performance was expected to be enhanced due to the modification of surface energy, morphology, and energy barrier between the ZnO based cathode and photoactive layer.

2. Experimental

2.1 Materials

Graphite (particle size < 20 μm), potassium permanganate, sodium nitrate, silver nitrate ($AgNO_3$), sodium boronhydride ($NaBH_4$), stearyl alcohol, isobutyryl chloride, methylene di-*p*-phenyl diisocyanate (MDI), poly(3-hexylthiophene) (P3HT), triethylamine (TEA), diethylenetriamine (DETA), *N*,*N*-dimethylformamide (DMF), cyclohexane, methanol, tetrahydrofuran (THF), xylene, sulfuric acid, and hydrogen peroxide were purchased from Aldrich, Acros, and Showa. [6,6]-Phenyl-C_{61}-butyric acid methyl ester ($PC_{61}BM$) was purchased from Nano-C and used as received. Polyethyleneimine (PEI, Mw = 70000 g/mol) was purchased from Sigma-Aldrich and used as received. Poly(oxyalkylene)amine Jeffamine® ED-2003 (abbreviated as ED2003) was purchased from Huntsman. The dendrons with different generations (from [G0.5]-C18 to [G2.5]-C18) were prepared by grafting stearyl alcohol onto the building block, IDD as described in previous reports (Figure 1) [56-59]. The layered graphene oxide (GO) was prepared in a rapid and relatively safe manner using modified Hummers method [60].

2.2 Preparation of exfoliated graphene nanosheets (XGS)

Graphene oxide (0.45 g) was dispersed in DI water (500 mL, pH ~ 3) and sonicated for 1 h at room temperature. Subsequently, the solution was heated at 95 °C for 72 h, and DI water was added periodically to compensate the loss due to evaporation. Exfoliated graphene nanosheets (XGS) were obtained after water evaporation [47].

2.3 Preparation of XGS-IDD

As illustrated in Scheme 1, XGS (0.10 g) was added to a solution of IDD (1.28 g, 4.00 mmol) in dry THF (10.0 mL). The solution was stirred at 75 °C under a N_2 atmosphere for 24 h. The black powder product XGS-IDD was obtained from the solution after washing with acetone and DI water for four times, and then dried by using a freeze dryer. FT-IR (ν_{max}/cm^{-1}): 1855, 1774 (C=O, azetidine-2,4-dione), 1737 (C=O, urethane).

2.4 Preparation of XGS-amine

As illustrated in Scheme 1, XGS-IDD (0.10 g) was added to a solution of ED2003 (10.0 g, 5.00 mmol) in dry THF (10.0 mL). The solution was stirred at 75 °C under a N_2 atmosphere for 72 h. The black powder product of ED2003-functionalized XGS with terminal amino groups (XGS-amine) was obtained from the solution after washing with acetone and DI water for four times and dried by using a freeze dryer. FT-IR (ν_{max}/cm^{-1}): 3361, 3190 (NH_2), 1656 (C=O, malonamide).

2.5 Preparation of XGS-dendritic derivatives

The XGS-dendritic derivatives (XGS-G0.5, XGS-G1.5, and XGS-G2.5) were prepared through the reaction of XGS-amine and dendrons. Detail reaction procedure was described as follows:

2.5.1 Preparation of XGS-G0.5

As illustrated in Scheme 1, XGS-amine (0.10 g) was added to a solution of [G0.5]-C18 (2.36 g, 4.00 mmol) in dry THF (10 mL). The solution was stirred at 75 °C under a N_2 atmosphere for 24 h. The black powder product XGS-G0.5 was obtained from the solution after washing with THF and DI water

for four times, and then dried by using a freeze dryer. FT-IR (ν_{max}/cm^{-1}): 1730 (C=O, urethane), 1645 (C=O, malonamide).

2.5.2 Preparation of XGS-G1.5

As illustrated in Scheme 1, XGS-amine (0.10 g) was added to a solution of [G1.5]-C18 (6.42 g, 4.00 mmol) in dry THF (15 mL). The solution was stirred at 75 °C under a N_2 atmosphere for 24 h. The black powder product XGS-G1.5 was obtained from the solution after washing with THF and DI water for four times, and then dried by using a freeze dryer. FT-IR (ν_{max}/cm^{-1}): 1728 (C=O, urethane), 1644 (C=O, malonamide).

2.5.3 Preparation of XGS-G2.5

As illustrated in Scheme 1, XGS-amine (0.10 g) was added to a solution of [G2.5]-C18 (14.6 g, 4.00 mmol) in dry DMF (15 mL). The solution was stirred at 75 °C under a N_2 atmosphere for 24 h. The black powder product XGS-G2.5 was obtained from the solution after washing with DMF and DI water for four times, and then dried by using a freeze dryer. FT-IR (ν_{max}/cm^{-1}): 1733 (C=O, urethane), 1646 (C=O, malonamide).

2.6 Preparation of XGS-G2.5/AgNPs

As illustrated in Scheme 2, the procedures for the preparation of the XGS-G2.5/AgNPs nanohybrids were described below: XGS-G2.5 (0.05 g) was added to $AgNO_3$ (0.01 g, 0.60 mmol) dissolved in THF/DI water (4:1, v/v) solution (500 mL). Under N_2 atmosphere, $NaBH_4$ (0.05 g, 1.20 mmol) dissolved in THF/DI water (4:1, v/v) solution (500 mL) was added to the XGS-G2.5 mixture dropwise under vigorous stirring. The proceeding of the reduction of Ag^+ to Ag^0 was indicated by the color change of the reaction mixture from transparent to yellow.

2.7 Fabrication and characterization of inverted PSCs

All the inverted PSCs in this study were based on a structure consisting of indium tin oxide (ITO)-coated glass/ZnO/interfacial layer/photoactive layer/MoO_3 (5 nm)/Ag (50 nm), in which the photoactive layer comprised an interpenetrating network of P3HT/PC_{61}BM [61, 62]. The ITO substrates

(Sanyo, Japan (8 Ω □$^{-1}$)) were first patterned by lithography, cleaned with detergent, ultra-sonicated in acetone and isopropyl alcohol, dried on a hot plate at 120 °C for 5 min, and finally treated with oxygen plasma for 5 min. A ZnO precursor solution was spin-cast on a pre-cleaned ITO-glass substrate and annealed at 200 °C for 1 h to give a ZnO film with a thickness of 30 nm, as determined by profilometer [15]. The PEI/XGS-G2.5 or PEI/XGS-G2.5/AgNPs solution was prepared by the mixing of PEI solution (0.4 wt.% in methoxyethanol) and XGS-G2.5 or XGS-G2.5/AgNPs solution (0.1 wt% in methoxyethanol) under vigorous stirring (1:1, v/v). The PEI/XGS-G2.5 or PEI/XGS-G2.5/AgNPs solution was then spin-coated (5000 rpm) on the ZnO-coated substrates to afford a bilayer film after being annealed at 120 °C for 10 min. In addition, an o-DCB solution of P3HT/$PC_{61}BM$ (10 mg mL^{-1}) was stirred overnight, then filtered through a 0.2 μm poly(tetrafluoroethylene) filter, and spin-coated (1200 rpm, 30 s) onto the PEI/XGS-G2.5 or PEI/XGS-G2.5/AgNPs based interfacial layer to form the P3HT/$PC_{61}BM$ (1: 0.8, w/w) blend film-based photo-active layer. The thickness of the photo-active layer was ca. 60 nm. Subsequently, a thin MoO_3 layer with a thickness of approximately 5 nm was vacuum-deposited on the top of the photoactive layer with an evaporation rate of 0.1 Å s^{-1}. In addition, the top electrode Ag (50 nm) was thermally deposited through a shade mask with an effective device area of 3 mm^2. Finally the cell was encapsulated using UV-curing glue (Nagase, Japan) in the glove box. The PV performance of the PSC devices were measured in an ambient atmosphere at 25 °C using a computer-controlled Keithley 2400 source measurement unit (SMU) equipped with a Peccell solar simulator under AM 1.5G illumination (100 mW cm^{-2}). The illumination intensity was calibrated using a standard Si photodiode detector equipped with a KG-5 filter. The output photocurrent was adjusted to match the photocurrent of the Si reference cell to obtain a power density of 100 mW cm^{-2}.

2.8 Measurement

FTIR spectra were recorded using a Jasco 4100 FTIR spectrometer. Thermogravimetric analysis (TGA) was performed by using a TA Instruments Q50 thermogravimetric analyzer operated at a heating rate of 10 °C/min under N_2. Thermal decomposition temperature (T_d) was taken to be the temperature

corresponding to 5% weight loss of the sample. Transmission electron microscopy (TEM) was performed on a JOEL JEM-1230 with Gatan Dual Vision CCD Camera and operated at 120 kV, and the solution was dipped on a 200 mesh carbon-coated Cu grid for the analyses. X-ray diffraction (XRD) analysis was performed by using a Rigaku D/MAX-2200 PC diffractometer with a Cu target (λ = 1.542 Å), operated at a scanning rate of 2°/min. The d-spacing of the samples was analyzed by Bragg's equation ($n\lambda = 2d\sin\theta$). X-ray photoelectron spectroscopy (XPS) was recorded by using a VG Scientific ESCALAB 250 spectrometer. The contact angles (CAs) of water droplets (5 mL) on the films were measured at room temperature at 5-s intervals for 30 s using an optical contact angle meter (Kyowa DropMaster); all the measured CAs were constant during the 30-s period. The work functions of the thin films based on XGS-G2.5 were determined using atmospheric photoelectron spectroscopy (RIKEN Keiki AC2).

3. Results and discussion

3.1. Preparation and characterization of the exfoliated graphene nanosheets (XGS)

Graphene oxide (GO) was synthesized from graphite by Hummer's method [60] and characterized in the same manner as that in our previous study [63]. The prepared GO was further reduced in acidic DI water (pH ~ 3) at 95 °C and exfoliated into single layer graphene sheets (XGS) by the hydrazine-free method reported by Liao et al. [47]. The d-spacings of GO and exfoliated XGS were measured by wide-angle X-ray diffraction (WXRD). The diffraction pattern shows that GO had a strong diffraction peak at $2\theta = 11.3^{o}$, corresponding to a d-spacing of 7.83 Å (Figure 2). For XGS, the absence of diffraction peaks indicates that the graphene sheets were exfoliated. According to the literature [64], the exfoliation of GO was achieved by the extra pressure exerted from the externally heated, volatile hydrochloric acid. XGS and GO were further characterized by X-ray photoelectron spectroscopy (XPS). As shown in Figure 3, C1s spectra indicate that the superpositions of multiple strong peaks were observed at 284.0-294.0 eV for both GO and XGS. The spectrum of GO exhibited characteristic peaks at 284.2, 286.2, 286.8, and 288.0 eV, corresponding to C=C (sp^2), C-O (epoxy), C-OH, and

COOH functionalities, respectively (Figure 3(a)). In the case of XGS, a red shift was occurred in the peak positions. XPS analysis also reveals that the XGS possessed lower relative percentages of C-O bond (9.2 %) and COOH group (3.5 %) than those of GO (21 and 11.3 %, respectively) (Figure 3(b)). The reduction of oxygen and simultaneous transformation of the sp^3 carbon into sp^2 carbon are attributed to the dehydration of exfoliated GO from the condensation reaction between a hydroxyl group (OH) and a hydrogen atom (H) attaching to two neighboring carbons in an acidic environment. Furthermore, the higher C/O atomic ratio for XGS (3.6) than that for GO (2.0) implies that only partial reduction of oxygen atoms was occurred during the exfoliation process. As shown in Figure 4, Raman spectra show that the G bands of GO and XGS appeared at 1604 and 1596 cm^{-1}, respectively. Since the values are close to 1579 cm^{-1} of the pristine graphite [64], the successful reduction of GO was indeed achieved [65, 66]. Furthermore, it was reported that the ordered and disordered crystal structures of carbon were closely related to the content of sp^2 carbons and correlated to the intensity ratio D/G [67]. Thus, the decrease in the D/G of XGS from 2.14 to 1.94 is attributed to the increase in the content of sp^2 carbon upon reduction.

3.2. Synthesis and characterization of XGS-dendritic derivatives

In order to promote organic compatibility, XGS were chemically modified to afford XGS-dendritic derivatives (XGS-G0.5, XGS-G1.5, and XGS-G2.5) in a three-step procedure as shown in Scheme 1. First, the hydroxyl and carboxyl (COOH) groups of XGS were allowed to react with the isocyanate functionality of IDD to form XGS-IDD. FT-IR spectra in Figure 5(a) reveal that XGS exhibited characteristic absorption peaks at wavelength 1737 cm^{-1} for the formation of the urethane functionality, and 1774 and 1855 cm^{-1} for the presence of azetidine-2,4-dione unit. The absence of absorption peaks for the isocyanate functionality (ν = 2260 cm^{-1}) of IDD, and carboxylic groups (ν = 3283 and 1706 cm^{-1}) for XGS further verified the completion of reaction. The XGS-IDD subsequently underwent a ring-opening reaction of the azetidine-2,4-dione group by using the hydrophilic poly(oxyalkylene)amine ED2003 to afford the intermediate XGS-amine with characteristic absorption peaks at 1656 cm^{-1} for the malonamide units, and 3190 and 3361 cm^{-1} for the NH_2 functionality (Figure 5b)). In addition to

providing a change of functionality, ED2003 could serve as an excellent compatibilizer between organic moiety and inorganic component due to the presence of a large number of oxyethylene units [68]. The XGS-amines were further reacted with dendrons of various generations to give the XGS-dendritic derivatives (XGS-G0.5, XGS-G1.5, and XGS-G2.5) with characteristic absorption peaks at 1646 and 1733 cm^{-1} for the malonamide and urethane groups, respectively (Figure 5(c)). The dendrons featured a focal part rich in hydrogen bonding sites, and peripheral nonpolar units offering van der Waals interactions, thus capable of providing more organic compatibility.

Thermogravimetric analysis of the dendritic derivatives showed that the thermal decomposition temperatures, T_ds ranged from 229 to 241 °C (Table 1). Since the decomposition of organics usually occurs above 200 °C [69], the organic fraction determined from the percentage of weight loss between the temperatures ranged from 200 to 600 °C. As shown in Figure S1 (supporting information), 25 wt% loss was observed at 600 ^{o}C for XGS, which corresponds to the degradation of organic fraction. Moreover, the weight losses of XGS-0.5, XGS-1.5, and XGS-2.5 were about 62, 46, and 36 wt%, respectively. Taking into account the weight loss of XGS (25%), we roughly assigned the weight loss values of 37, 21, and 11 wt% from XGS-0.5, XGS-1.5, and XGS-2.5, respectively, to the degradation of its linear dendritic segments. The results indicate that the derivatives have a decrease in organic fraction from 37 wt% in XGS-G0.5 to 11 wt% in XGS-G2.5. The low organic content in the high generation dendron grafted XGS could be attributed to the difficulty to graft the rather bulky dendrons because of steric hindrance. Moreover, the XGS-dendritic derivative with a higher content of organic fraction exhibited a lower char yield.

3.3. Morphologies of the XGS-dendritic derivatives and XGS-G2.5/AgNPs nanohybrid

The d-spacings of XGS-dendritic derivatives were measured by XRD. As shown in Figure 2, a diffraction peak at $2\theta = 11.3^{o}$ was present in the XRD pattern for GO, corresponding to a d-spacing of 7.83 Å. For XGS and XGS-dendritic derivatives, a featureless pattern was observed, implying that all the nanosheets were exfoliated. We further utilized TEM to confirm the results based on the XRD study. TEM images and electron diffraction patterns (SAED) are shown in the insets of Figure 6.

TEM image shows that GO possessed a stack-layered structure, yet the SAED pattern featured only weak and diffuse rings, indicating the loss of long-range ordering in the structure (Figure 6 (a)). The deterioration of the regular stacking of GO layers resulted in the poor electron diffraction of the GO sample. Moreover, the electron diffraction pattern became more distinct for the XGS sample (Figure 6(b)). More ordered structure was formed as a result of the reduction of oxygen and simultaneous transformation of the carbon sp^3 bonds into sp^2 for the XGS sample. In addition, the strong diffraction spots were observed for the XGS-G0.5 (Figure 6 (c)). These results indicate the formation of a hexagonal crystalline structure for XGS-G0.5. The SAED patterns of XGS-G1.5 and XGS-G2.5 featured a ring of diffraction spots with double 6-fold symmetry (Figure 6 (d) to (e)). The relative intensity of the inner 1100-type and outer 2110-type reflections were consistent with the presence of the single-layered graphene structure. [47, 70, 71]. On the basis of the above observations, the layered graphene sheets were completely exfoliated to yield folded single-layered XGS surrounded by dendritic derivatives. Apart from that, Ag^+ ions were reduced by using $NaBH_4$ to obtain Ag^0 chelated to XGS-G2.5, i.e. XGS-G2.5/AgNPs (Scheme 2). TEM image indicates that the spherical AgNPs exhibited an average diameter of approximately 5–10 nm and distributed uniformly on the surface of XGS possibly due to the presence of the dendritic template (Figure 6(f)). The content of AgNPs was characterized by using TGA. The char yield of the XGS-G2.5/AgNPs nanohybrid indicates that 8.6 wt.% of AgNPs was dispersed in the XGS-G2.5 sample. Moreover, the crystallinity of AgNPs in XGS-G2.5/AgNPs nanohybrid has been confirmed by X-ray diffractometer. As shown in Figure S2 (supporting information), X-ray diffraction pattern indicates that four diffraction peaks corresponding to the (1 1 1), (2 0 0), (2 2 0), and (3 1 1) crystalline planes of AgNPs were present at θ = 37.9◦, 44.2◦, 64.4◦, and 77.2◦, respectively. Indeed, the crystalline nanoparticles are present in nanohybrids.

3.4 Surface energy of the PEI/XGS-G2.5 and PEI/XGS-G2.5/AgNPs coated ZnO layer

According to the literature [32], the surface energy of ZnO would significantly influence the compatibility between the ZnO layer and conjugated polymer based photoactive layer. Moreover, the PV performance of inverted PSC was closely related to the surface energy of ZnO layer. The PV

performance was further influenced by controlling the surface energy of a surface modified ZnO buffer layer. The best PV performance of P3HT:$PC_{61}BM$ based inverted PSC was obtained as the intermediate surface energy was found to be 51 mN/m for the surface modified ZnO layer [32]. Thus, we calculated the surface free energies of the ZnO layer, P3HT, and PEI/XGS-G2.5 and PEI/XGS-G2.5/AgNPs coated ZnO layer by measuring their contact angles (CAs) to water and glycerol based on Wu's model (Harmonic mean) [32]. The measured CA values (θ) were input into the following equations to calculate the polar (γ^p) and dispersive (γ^d) components of the total energy γ^{tot}, where subscript w referred to deionized water and Gly to glycerol:

$\gamma_w (1 + \cos\theta_w) = [4\gamma_w^d\gamma^d / (\gamma_w^d + \gamma^d)] + [4\gamma_w^p\gamma^p / (\gamma_w^p + \gamma^p)]$, and

$\gamma_{Gly} (1 + \cos\theta_{Gly}) = [4\gamma_{Gly}^d\gamma^d / (\gamma_{Gly}^d + \gamma^d)] + [4\gamma_{Gly}^p\gamma^p / (\gamma_{Gly}^p + \gamma^p)]$.

Thus, the total surface energy is: $\gamma^{tot} = \gamma^p + \gamma^d$.

The calculation results of are summarized in Table 2. The surface energies of ZnO and P3HT were determined to be 71.4 and 20.0 mN/m, respectively, which are in good agreement with those reported in the literature [32]. The PEI/XGS-G2.5 and PEI/XGS-G2.5/AgNPs coated ZnO films exhibited surface energies of 63.8 and 63.5 mN/m, respectively. The surface energy of ZnO was decreased significantly as its surface was further modified by PEI/XGS-G2.5 or PEI/XGS-G2.5/AgNPs film. This is favorable for the improved compatibility between the ZnO layer and P3HT based photoactive layer. In addition, the surface energies of PEI/XGS-G2.5 and PEI/XGS-G2.5/AgNPs films were almost the same. The incorporation of AgNPs into the XGS-G2.5 film caused a very minor drop in the surface energy. This is because the nanoparticles were embedded in the nanohybrid rather than on the surface of XGS-G2.5.

3.6 Morphologies of the PEI/XGS-G2.5 and PEI/XGS-G2.5/AgNPs coated ZnO layers.

Electron-injection capacity and PV performance are strongly dependent on the morphology of the ZnO layer in inverted PSCs. AFM was utilized to investigate the surface morphology (topographic and phase-contrast images) of the PEI/XGS-G2.5 and PEI/XGS-G2.5/AgNPs coated ZnO layers.

As shown in Figures 7(a) and (b), a surface roughness of 5.2 nm was observed for the ZnO layer. The surface roughness was reduced as the PEI/XGS-G2.5 (4.8 nm) or PEI/XGS-G2.5/AgNPs (4.5 nm) was coated onto the ZnO layer. Indeed, the surface morphology of ZnO layer was influenced by the modification using PEI/XGS-G2.5 or PEI/XGS-G2.5/AgNPs. Nevertheless, high surface area was remained for the PEI/XGS-G2.5 and PEI/XGS-G2.5/AgNPs coated ZnO layers. High contact area is favorable for the electron transfer from the photoactive layer to the ZnO layer. In addition, the P3HT/PC_{61}BM blend based photoactive layer was further coated on the surfaces of ZnO, and PEI/XGS-G2.5 and PEI/XGS-G2.5/AgNPs modified ZnO layer, respectively. The topographic and phase-contrast images are shown in Figure 8. The phase images indicate that the PC_{61}BM units and P3HT were phase-separated in nanoscale on the surfaces of both XGS nanohybrid coated ZnO layers. In fact, the PV performance of the bulk heterojunction solar cells is strongly dependent on the morphology of the P3HT/PC_{61}BM blend film. To avoid recombination of the excitons, the P/N heterojunction phase must be controlled at the nanoscale level [72]. A certain degree of phase separation is crucial for the efficient formation of free carriers to provide the optimal PV properties of PSCs. Apart from that, the presence of the high surface area of photoactive layer favors for the hole-transfer from photoactive layer to anode electrode.

3.6 Work functions of XGS, XGS-G2.5, and XGS-G2.5/AgNPs

In general, PV performance of inverted PSCs is closely related to the energy of the surface modified ZnO layer. Because of this, we measured the work functions of XGS, XGS-G2.5, and XGS-G2.5/AgNPs in air using an AC2 photoelectron spectrometer. Figure 9 presents the square root of the counting rate (CR) for the XGS based nano-hybrids plotted with respect to the photon energy. From the crossing point of the background and the yield line, we determined the work functions of XGS, XGS-G2.5, and XGS-G2.5/AgNPs to be 5.40, 4.98 and 4.72 eV, respectively. The work functions of XGS-G2.5 and XGS-G2.5/AgNPs were larger than that of ZnO (4.2 eV), yet close to the work function of ITO (from 4.7 to 5.2 eV). The work function was reduced as the dendritic derivative and AgNPs

were incorporated into XGS. Accordingly, XGS-G2.5 and XGS-G2.5/AgNPs exhibited the potential to serve as the surface modifier for the ZnO layer in inverted PSCs.

3.7. PV performance of the P3HT/$PC_{61}BM$-based inverted PSCs

Inverted PSCs were fabricated based on the composition ITO/ZnO (30 nm)/P3HT:$PC_{61}BM$/MoO_3 (5 nm)/Ag (50 nm), of which ITO and Ag acted as the cathode and the anode, respectively. We respectively inserted PEI, PEI/XGS-G2.5, and PEI/XGS-G2.5/AgNPs nanohybrid as the modifying layer between the ZnO and photoactive layer. A configuration schematic diagram and energy levels of each component in PSCs are shown in Figure 10 (a) and (b), respectively. The energy levels of XGS-G2.5 and XGS-G2.5/AgNPs are lower than that of ZnO. The energy level of ZnO would be tuned as XGS-G2.5 and XGS-G2.5/AgNPs were respectively coated on the surface of ZnO. PV performance of PSCs was measured under illumination with solar-simulating light (100 mW cm^{-2}) from an AM1.5 solar simulator. The current density–voltage (*J-V*) characteristics curves of the inverted PSCs are shown in Figure 11, and the photovoltaic parameters are summarized in Table 3. The controlled bare device exhibited a PCE of 3.38 % with an open-circuit voltage (V_{OC}) of 0.59 V, a short-circuit current (J_{sc}) of 10.04 A/cm^2, and a fill factor (FF) of 0.57. As the ZnO layer was modified with a PEI/XGS-G2.5, the PV performance of inverted PSC was decreased, regardless of the decreased surface energy of ZnO by the addition of PEI/XGS-G2.5 layer. The presence of the dendritic derivatives in XGS decreased the conductivity and charge transfer capacity between the interface of ZnO and photoactive layer. On the other hand, the incorporation of the PEI/XGS-G2.5/AgNPs afforded an increase in J_{sc} (10.27 mA/cm^2) and FF (0.63). The PCE of PSC based on the ZnO layer modified with PEI/XGS-G2.5/AgNPs was significantly enhanced to 4.04 %, a 19.5 % improvement over the 3.38 % of the bare inverted PSC sample. In order to clarify the positive role of XGS-G2.5/AgNPs in PSCs, PV properties of a PSC with interfacial layer of PEI were studied. This PEI based PSC exhibited a PCE of 3.67 % with a V_{OC} of 0.59 V, a J_{sc} of 11.30 mA/cm^2, and a FF of 0.55. As compared to the controlled bare device, the PEI based PSC exhibited a lower FF value, and higher J_{sc} and PCE values. This implies that part of photocurrent resulted from the dark current of

PSC. As a result, a lower FF value was observed for the PEI based PSC. It is important to note that the addition of PEI based interfacial layer can achieved about 8.6 % improvement of PCE value for a P3HT:$PC_{61}BM$ based inverted cell. Based on this, the XGS-G2.5/AgNPs does play a positive role in the electron selective layer of inverted PSC. The addition of PEI/XGS-G2.5/AgNPs would reduce the surface roughness and energy level of the ZnO layer. Moreover, the presence of AgNPs in XGS-G2.5 increased the conductivity and charge transfer capacity between the interface of ZnO and photoactive layer. Consequently, higher photocurrent density and PCE value were observed for the PSC based on the PEI/XGS-G2.5/AgNPs modified ZnO layer. Apart from that, the improvement of PV properties might be contributed from the localized surface plasmon resonance (LSPR) of the AgNPs at the interface of ZnO and photoactive layer [46]. In order to confirm the LSPR effect of AgNPs, UV-vis absorption spectra of the P3HT coated ZnO, and P3HT and electron-selective layer (PEI/XGS-G2.5 or PEI/XGS-G2.5/AgNPs) coated ZnO layers were investigated. As shown in Figure 12, the absorption intensities were enhanced for the P3HT/ZnO films respectively inserted with PEI/XGS-G2.5 and PEIEPEI/XGS-G2.5/AgNPs when compared with that of the bare P3HT/ZnO film. Moreover, the absorption band was red-shifted for the P3HT/ZnO films incorporated with these electron-selective layers. Shahjamali et al. reported that the AgNPs with LSPR wavelength in the range 500-600 nm would enhance light absorption in the photo-active layer of PSC [46]. In addition, the enhancement of light absorption intensity of vibronic shoulder for P3HT might be due to the aggregation of polymer chains on PEI/XGS-G2.5/AgNPs layer. Therefore, the enhancement of PV performance was partially attributed to the LSPR effect of AgNPs and the morphology modification of P3HT based active layer.

4. Conclusion

We have successfully synthesized the exfoliated graphene nanosheets (XGS) from graphite. Subsequently, XGS-dendritic derivatives (XGS-G0.5, XGS-G1.5, and XGS-G2.5) were prepared by first grafting with dual-functional IDD compounds and subsequent coupling with poly(oxyalkylene)amine, followed by the covalent incorporation of various hydrophobic dendrons.

Moreover, the XGS-G2.5/AgNPs nanohybrid with well dispersed AgNPs was prepared. The PEI/XGS-G2.5 and PEI/XGS-G2.5/AgNPs nanohybrids were used as the interfacial layer between the ZnO and photoactive layer for the preparation of high-performance PSC. The incorporation of PEI/XGS-G2.5/AgNPs nanohybrid rendered the inverted PSC an increased power conversion efficiency to 4.04 %, a 19.5 % improvement over the 3.38 % of the bare inverted PSC, which is partially attributed to the LSPR effect of AgNPs. Moreover, the presence of PEI/XGS-G2.5/AgNPs improved the compatibility and charge transfer capacity between the interface of ZnO and photoactive layer. Therefore, higher photocurrent density and PCE value were observed for the inverted PSC based on the PEI/XGS-G2.5/AgNPs modified ZnO layer.

Acknowledgments

We thank the Chung-Shan Institute of Technology and the Ministry of Science and Technology (MOST) of Taiwan for financial support.

References

1. Y. J. Cheng, S. H. Yang and C. S. Hsu, *Chem. Rev.*, 2009, **109**, 5868.
2. J. T. Chen and C. S. Hsu, *Polym. Chem.*, 2011, **2**, 2707.
3. Y. Liang, Z. Xu, J. Xia, S. T. Tsai, Y. Wu, G. Li, C. Ray and L. Yu, *Adv. Mater.*, 2010, **22**, E135.
4. Y. Liang, D. Feng, Y. Wu, S. T. Tsai, G. Li, C. Ray and L. Yu, *J. Am. Chem. Soc.*, 2009, **131**, 7792.
5. S. H. Park, A. Roy, S. Beaupre, S. Cho, N. Coates, J. S. Moon, D. Moses, M. Leclerc, K. Lee and A. J. Heeger, *Nat. Photonics*, 2009, **3**, 297.
6. Y. Liang and L. Yu, *Acc. Chem. Res.*, 2010, **49**, 1227.
7. H. Y. Chen, J. H. Hou, S. Q. Zhang, Y. Y. Liang, G. Yang, Y. Yang, L. Yu, Y. Wu and G. Li, *Nat Photonics*, 2009, **3**, 649.
8. L. J. Huo, S. Q. Zhang, X. Guo, F. Xu, Y. F. Li, J. H. Hou, *Angew. Chem. Int. Ed.*, 2011, **50**, 9697.
9. H. J. Wang, L. H. Chan, C. P. Chen, S. L. Lin, R. H. Lee and R. J. Jeng, *Polymer*, 2011, **52**, 326.
10. R. H. Lee, J. Y. Syu and J. L. Huang, *Polym. Adv. Technol.*, 2011, **22**, 2110.
11. H. J. Wang, Y. P. Chen, Y. C. Chen, C. P. Chen, R. H. Lee, L. H. Chan and R. J. Jeng, *Polymer*, 2012, **53**, 4091.
12. R. H. Lee, J. L. Huang and C. H. Chi, *J. Polym. Sci: Polym. Phys.*, 2013, **51**, 137.
13. F. C. Krebs and K. Norman, *Prog. Photovolt.*, 2007, **15**, 697.

14. M. Jorgensen, K. Norman and F. C. Krebs, *Solar energy Mater. Solar Cell*, 2008, **92**, 686.
15. H. J. Wang, C. W. Chou, C. P. Chen, Y. H. Chen, R. H. Lee and R. J. Jeng, *J. Mater. Chem. A*, 2013, **1**, 8950.
16. M. J. Tan, S. Zhong, J. Li, Z. Chen, W. Chen, *ACS Appl. Mater. Interfaces*, 2013, **5**, 4696.
17. R. Peng, F. Yang, X. Ouyang, Y. Liu, Y. S. Kim, Z. Ge, *Appl. Phys. A*, 2014, **114**, 429.
18. S. K. Hau, H. L. Yip, N. S. Baek, J. Zou, K. O'Malley and A. K. Y. Jen, *Appl. Phys. Lett.*, 2008, **92**, 253301.
19. Y. M. Sung, F. C. Hsu and Y. F. Chen, *Solar energy Mater. Solar Cell*, 2014, **125**, 239.
20. J. Xiong, J. Yang, B. Yang, C. Zhou, X. Hu, H. Xie, H. Huang and Y. Gao, *Org. Electron.*, 2014, **15**, 1745.
21. Z. Yuan, *J. Mater. Sci.: Mater. Electron.*, 2014, **25**, 1289.
22. W. Qin, G. Ding, X. Xu, L. Yang and S. Yin, *J. Mater. Sci. Technol.*, 2014, **30**, 197.
23. G. K. Mor, K. Shankar, M. Paulose, O. K. Varghese and C. A. Grimes, *Appl. Phys. Lett.*, 2007, **91**, 15211
24. Z. Lin, J. Chang, J. Zhang, C. Jiang, J. Wu and C. Zhu, *J. Mater. Chem.*, 2014, **2**, 7788.
25. H. Kang, S. Hong, J. Lee and K. Lee, *Adv. Mater.*, 2012, **24**, 3005.
26. A. K. K. Kyaw, D. H. Wang, V. Gupta, J. Zhang, S. Chand, G. C. Bazan and A. J. Heeger, *Adv. Mater.*, 2013, **25**, 2397.
27. Y. Zhou, C. F. Hernandez, J. Shim, J. Meyer, A. J. Giordano, H. Li, P. Winget, T. Papadopoulos, H. Cheun, J. Kim, M. Fenoll, A. Dindar, W. Haske, E. Najafabadi, T. M. Khan, H. Sojoudi, S. Barlow, S. Graham, J. L. Bredas, S. R. Marder, A. Kahn and B. Kippelen, Science, 2012, **336**, 327.
28. T. Hu, F. Li, K. Yuan and Y. Chen, *ACS Appl. Mater. Interfaces*, 2013, **5**, 5763.
29. C. Xie, L. Chen and Y. Chen, *J. Phys. Chem. C*, 2013, **117**, 24804.
30. S. Zhong, R. Wang, H. Y. Mao, Z. He, H. Wu and W. Chen, *J. Appl. Phys.*, 2013, **114**, 113709.
31. S. Liu, K. Zhang, J. Lu, J. Zhang, H. L. Yip, F. Huang and Y. Cao, *J. Am. Chem. Soc.*, 2013, **135**, 15326.
32. X. Bulliard , S. G. Ihn , S. Yun , Y. Kim , D. Choi , J. Y. Choi , M. Kim , M. Sim , J. H. Park , W. Choi and K. Cho, *Adv. Funct. Mater.*, 2010, **20**, 4381.
33. F. Zhu, X. Chen, Z. Lu, J. Yang, S. Huang and Z. Sun, *Nano. Micro. Lett.*, 2014, **6**, 24.
34. S. Cho, K. D. Kim, J. Heo, J. Y. Lee, G. Cha, B. Y. Seo, Y. D. Kim, Y. S. Kim, S. Y. Choi and D. C. Lim, *Scientific Reports*, 2014, **4**, 4306.
35. S. K. Hau, H. L. Yip, O. Acton, N. S. Baek, H. Ma and A. K. Y. Jen, *J. Mater. Chem.*, 2008, **18**, 5113.

36. P. Li, X. Li, C. Sun, G. Wang, J. Li, T. Jiu and J. Fang, *Solar energy Mater. Solar Cell*, 2014, **126**, 36.
37. H. Choi, J. Lee, W. Lee, S. J. Ko, R. Yang, J. C. Lee, H. Y. Woo, C. Yang and J. Y. Kim, *Org. Electron.*, 2013, **14**, 3138.
38. S. K. Hau, Y. J. Cheng, H. L. Yip, Y. Zhang, H. Ma and A. K. Y. Jen, *ACS Appl. Mater. Interfaces*, 2010, **2**, 1892.
39. H. L. Yip and A. K. Y. Jen, *Energy Environ. Sci.*, 2012, **5**, 5994.
40. H. B. Yang, Y. Q. Dong, X. Wang, S. Y. Khoo and B. Liu, *Solar energy Mater. Solar Cell*, 2013, **117**, 214.
41. H. W. Lee, J. Y. Oh, T. I. Lee, W. S. Jang, Y. B. Yoo, S. S. Chae, J. H. Park, J. M. Myoung, K. M. Song and H. K. Baik, *Appl. Phys. Lett.*, 2013, **102**, 193903.
42. Y. Zhang, S. Yuan, Y. Li and W. Zhang, *Electrochim. Acta*, 2014, **117**, 438.
43. H. B. Yang, Y. Q. Dong, X. Wang, S. Y. Khoo and B. Liu, *ACS Appl. Mater. Interfaces*, 2014, **6**, 1092.
44. F. Xie, W. C. H. Choy, W. E. I. Sha, D. Zhang, S. Zhang, X. Li, C. W. Leung and J. Hou, *Energy Environ. Sci.*, 2013, **6**, 3372.
45. X. Li, W. C. H. Choy, F. Xie, S, Zhang and J. Hou, *J. Mater. Chem. A*, 2013, **1**, 6614.
46. M. M. Shahjamali, M. Salvador, M. Bosman, D. S. Ginger, C. Xue, *J. Phys. Chem. C*, 2014, **118**, 12459.
47. K. H. Liao, A. Mittal, S. Bose, C. Leighton, K. A. Mkhoyan and C. W. Macosko, *ACS Nano*, 2011, **5**, 1253.
48. C. P. Chen, S. A. Dai, H. L. Chang, W. C. Su and R. J. Jeng, *J. Polym. Sci., Part A: Polym. Chem.*, 2005, **43**, 682.
49. S. A. Dai, T. Y. Juang, C. P. Chen, H. Y. Chang, W. J. Kuo, W. C. Su and R. J. Jeng, *J. Appl. Polym. Sci.*, 2007, **103**, 3591.
50. S. M. Shau, T. Y. Juang, H. S. Lin, C. L. Huang, C. F. Hsieh, J. Y. Wu and R. J. Jeng, *Polym. Chem.*, 2012, **3**, 1249
51. C. C. Tsai, T. Y. Juang, S. A. Dai, T. M. Wu, W. C. Su, Y. L. Liu and R. J. Jeng, *J. Mater. Chem.*, 2006, **16**, 2056.
52. P. L. Kuo and W. F. Chen, *J. Phys. Chem. B*, 2003, **107**, 11267.
53. S. M. Shau, C. C. Chang, C. H. Lo, Y. C. Chen, T. Y. Juang, S. A. Dai, R. H. Lee and R. J. Jeng, *ACS Appl. Mater. Interfaces*, 2012, **4**, 1897.
54. H. W. Tien, Y. L. Huang, S. Y. Yang, J. Y. Wang and C. C. M. Ma, *Carbon*, 2011, **49**, 1550.

55. C. Ran, M. Wang, W. Gao, Z. Yang, J. Deng, J. Ding and X. Song, *Phys. Chem. Chem. Phys.*, 2014, **16**, 4561.
56. J. K. Liu, S. M. Shau, T. Y. Juang, C. C. Chang, S. A. Dai, W. C. Su, C. H. Lin and R. J. Jeng, *J. Appl. Polym. Sci.*, 2011, **120**, 2411.
57. H. L. Chang, T. Y. Chao, C. C. Yang, S. A. Dai and R. J. Jeng, *Eur. Polym. J.*, 2007, **43**, 3988.
58. T. Y. Juang, C. C. Tsai, T. M. Wu, S. A. Dai, C. P. Chen, J. J. Lin, Y. L. Liu and R. J. Jeng, *Nanotechnology*, 2007, **18**, 205606.
59. C. C. Tsai, C. C. Chang, C. S. Yu, S. A. Dai, T. M. Wu, W. C. Su, C. N. Chen, F. M. C. Chen and R. J. Jeng, *J. Mater. Chem.*, 2009, **19**, 8484
60. W. S. Hummers and R. E. Offeman, *J. Am. Chem. Soc.*, 1958, **80**, 1339.
61. C. P. Chen, Y. D. Chen and S. C. Chuang, *Adv. Mater.*, 2011, **23**, 3859.
62. H. J. Wang, C. W. Chou, C. P. Chen, Y. H. Chen, R. H. Lee and R. J. Jeng, *J. Mater. Chem. A*, 2013, **1**, 8950.
63. G. L. Chen, S, M. Shau, T. Y. Juang, R. H. Lee, C. P. Chen, S. Y. Suen and R. J. Jeng, *Langmuir*, 2011, **27**, 14563.
64. B. Shen, D. Lu, W. Zhai and W. Zheng, *J. Mater. Chem. C*, 2013, **1**, 50.
65. H. B. Zhang, J. W. Wang, Q. Yan, W. G. Zheng, C. Chen and Z. Z. Yu, *J. Mater. Chem.*, 2011, **21**, 5392.
66. S. Stankovich, R. D. Piner, S. T. Nguyen and R. S. Ruoff, *Carbon*, 2006, 44, 3342.
67. K. N. Kudin, B. Ozbas, H. C. Schniepp, R. K. Prud'homme, I. A. Aksay and R. Car, *Nano Lett.*, 2007, **8**, 36.
68. J. Y. Chiou, R. S. Hsu, C. W. Chiu and J. J. Lin, *RSC Adv.*, 2013, **3**, 12847.
69. R. H. Lee, C. H. Chi and Y. C. Hsu, *J. Nanopart. Res.*, 2013, 15, 1733.
70. J. C. Meyer, A. K. Geim, M. I. Katsnelson, K. S. Novoselov, D. Obergfell, S. Roth, C. Girit and A. Zettl, *Solid State Commun.*, 2007, **143**, 101.
71. S. S. Li, K. H. Tu, C. C. Lin, C. W. Chen, M. Chhowalla, *ACS Nano*, 2010, 4, 3169.
72. C. Y. Huang, W. H. Lee and R. H. Lee, *RSC Adv.*, 2014, **4,** 48150.

Figure captions

Table 1. Thermal properties of XGS and XGS-dendritic derivatives.

Table 2. Contact angles and surface energies for ZnO, PEI/XGS-G2.5, PEI/XGS-G2.5/AgNPs, and P3HT.

Table 3. Photovoltaic characteristics of PSCs modified with electron selective layer based on bare ZnO, PEI/XGS-G2.5 and PEI/XGS-G2.5/AgNPs coated ZnO layers.

Scheme 1. Three-step synthetic route for XGS-dendritic derivatives.

Scheme 2. Schematic representations of XGS-dendritic derivatives and XGS-dendritic derivatives/AgNPs.

Fig 1. Chemical structures of (a) [G0.5]-C18, (b) [G1.5]-C18, and (c) [G2.5]-C18.

Fig 2. XRD patterns of GO and XGS.

Fig 3. XPS spectra of (a) GO and (b) XGS.

Fig 4. Raman spectra of GO and XGS.

Fig 5. FT-IR spectra of (a) XGS-IDD, (b) XGS-amine, and (c) XGS-G2.5.

Fig 6. TEM images of GO, XGS, XGS-dendritic derivatives, and XGS-G2.5/AgNPs (Insets show electron diffraction patterns on selected area).

Fig 7. AFM tapping mode (a, c, e,) topographic and (b, d, f) phase images of ZnO (a, b), and PEI/XGS-G2.5 (c, d) and PEI/XGS-G2.5/AgNPs (e, f) coated ZnO films after annealing at 80 °C for 60 min.

Fig 8. AFM tapping mode (a, c, e,) topographic and (b, d, f) phase images of P3HT:$PC_{61}BM$ layer on the ZnO (a, b), PEI/XGS-G2.5 coated ZnO (c, d), and PEI/XGS-G2.5/AgNPs (e, f) coated ZnO layer annealing at 80 °C for 60 min.

Fig 9. Work functions of XGS, XGS-imine, XGS-G2.5, and XGS-G2.5/AgNPs.

Fig 10. (a) Device architecture of the P3HT/$PC_{61}BM$-based inverted PSCs using XGS-G2.5/AgNPs as a modifying layer. (b) Schematic illustration on the energy levels of each individual component in the PSCs.

Fig 11. Current density-potential curves of illuminated (AM 1.5G, 100 mW cm^{-2}) P3HT/$PC_{61}BM$-based inverted PSCs.

Figure 12. UV-Vis absorption spectra of the P3HT/ZnO, and PEI/XGS-G2.5 and PEI/XGS-G2.5/AgNPs inserted P3HT/ZnO films.

Table 1. Thermal properties of XGS and XGS-dendritic derivatives.

Sample	T_d[a] (°C)	Organic fraction[b] (wt%)	Char yield (wt%)
XGS	256	–	57.3
XGS-G0.5	229	37	26.5
XGS-G1.5	239	21	44.6
XGS-G2.5	241	11	57.6

[a] Temperature at which 5% weight loss occurred (N_2; heating rate: 10 °C/min).
[b] Taking into account the weight loss of XGS, organic fraction of XGS-dendritic derivatives determined from the percentage of weight loss between the temperatures ranged from 200 to 600 °C.

Table 2. Contact angles and surface energies for ZnO, PEI/XGS-G2.5, PEI/XGS-G2.5/AgNPs, and P3HT.

Films	θ_{water} (°)	$\theta_{glycerol}$ (°)	γ^p (mN/m)	γ^d (mN/m)	γ^{tot} (mN/m)
ZnO	39.3	59.7	67.8	3.64	71.4
ZnO/PEI/XGS-G2.5	38.3	50.0	55.3	8.52	63.8
ZnO/PEIXGS-G2.5/AgNPs	39.1	52.4	55.9	7.64	63.5
P3HT	104.3	94.2	5.6	14.4	20.0

[a] The measured contact angle values, θ, were input into the Wu equation (harmonic mean) to calculate the polar (γ^p) and dispersive (γ^d) components of the total energy γ^{tot}.

Table 3. Photovoltaic characteristics of PSCs modified with electron selective layer based on bare ZnO, and PEI, PEI/XGS-G2.5, and PEI/XGS-G2.5/AgNPs coated ZnO layers.

Modifying layer[a]	V_{oc} (v)	J_{sc} (mA/cm^2)	FF (%)	PCE (%)
Bare ZnO	0.59	10.04	0.57	3.38
ZnO/PEI	0.59	11.30	0.55	3.67
ZnO/PEI/XGS-G2.5	0.58	9.60	0.55	3.06
ZnO/PEI/XGS-G2.5/AgNPs	0.62	10.27	0.63	4.04

Enhanced Photovoltaic Performance of Inverted Polymer Solar Cells by Incorporating Graphene Nanosheet/AgNPs Nanohybrids

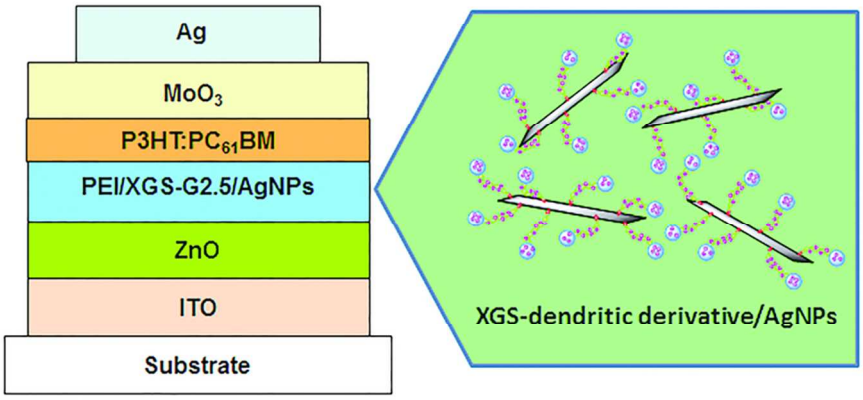

43x26mm (600 x 600 DPI)

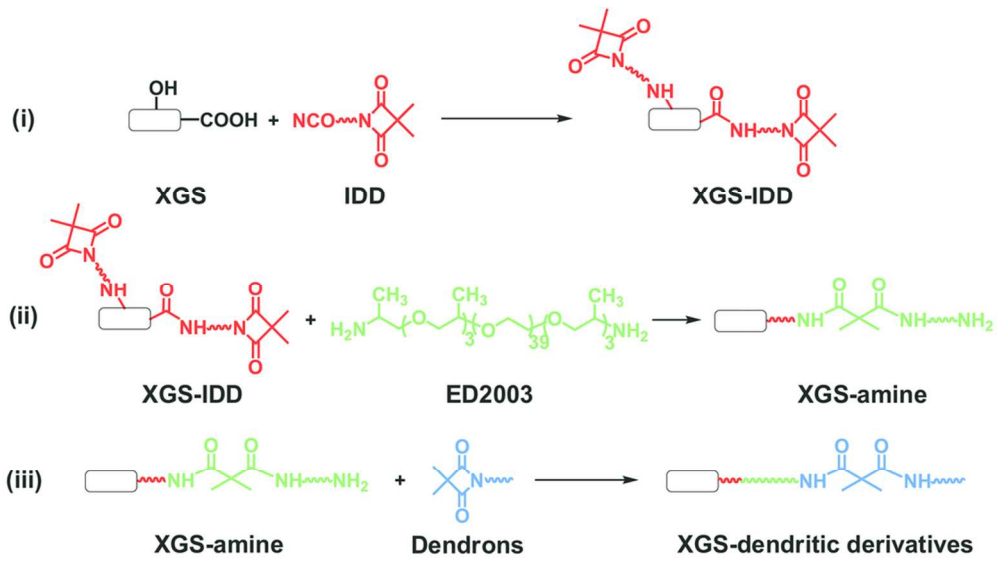

Three-step synthetic route for XGS-dendritic derivatives.
45x25mm (600 x 600 DPI)

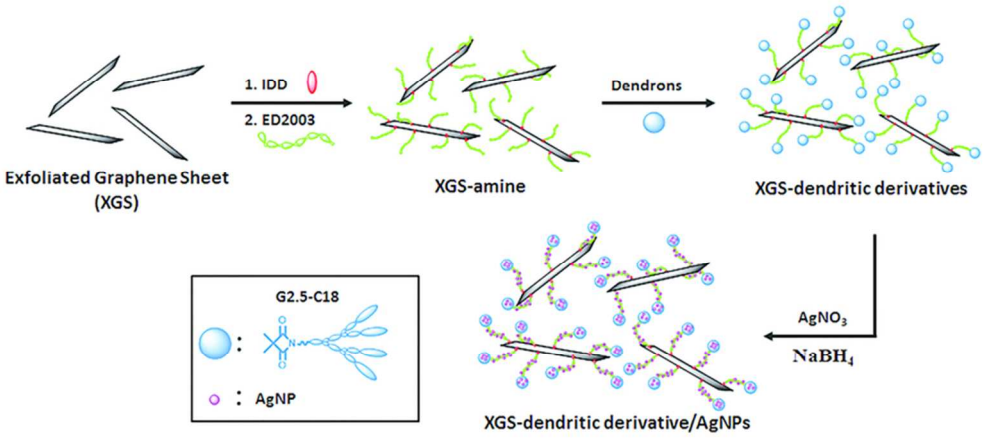

Schematic representations of XGS-dendritic derivatives and XGS-dendritic derivatives/AgNPs.
37x17mm (600 x 600 DPI)

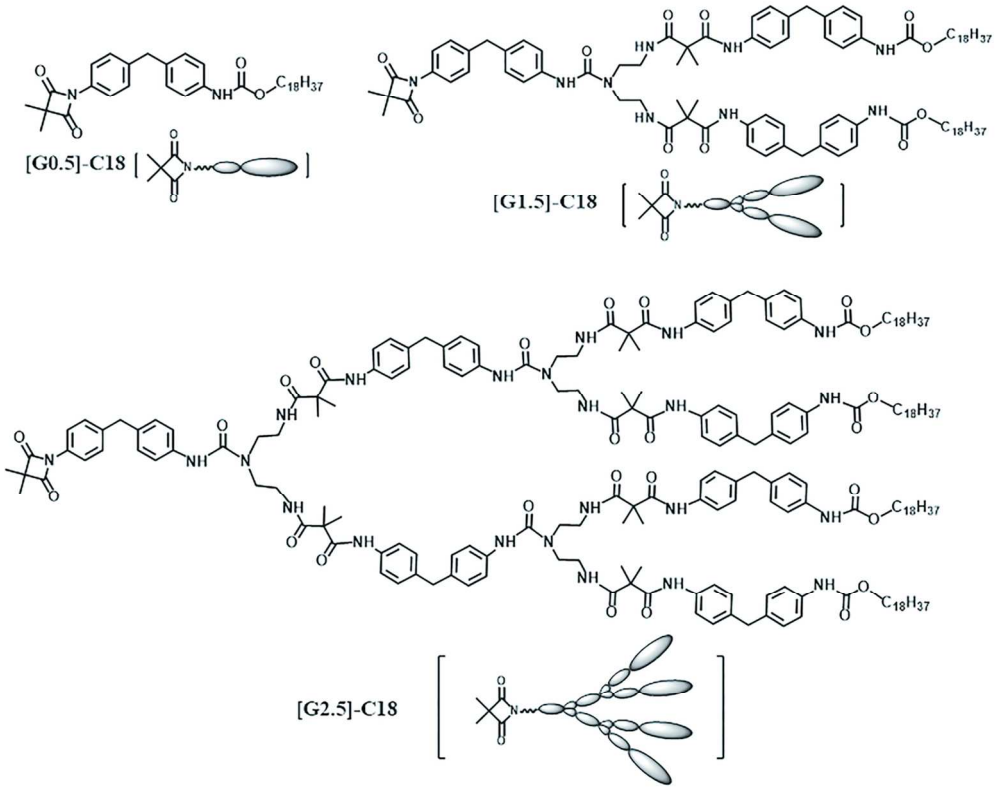

Chemical structures of (a) [G0.5]-C18, (b) [G1.5]-C18, and (c) [G2.5]-C18.
65x51mm (600 x 600 DPI)

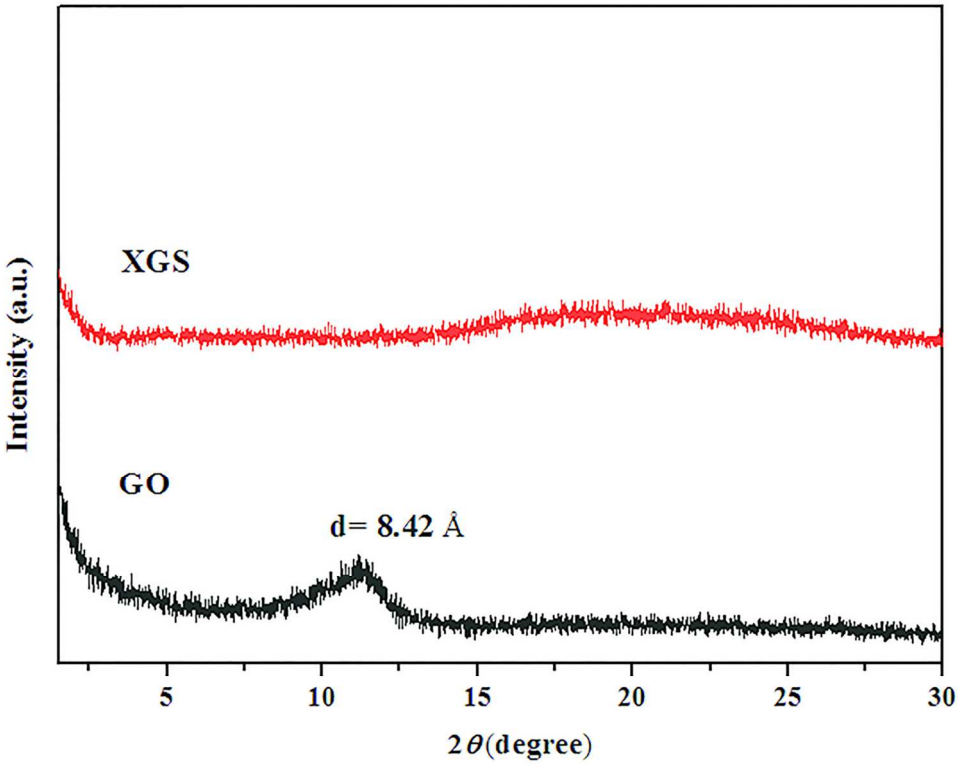

XRD patterns of GO and XGS.
65x52mm (600 x 600 DPI)

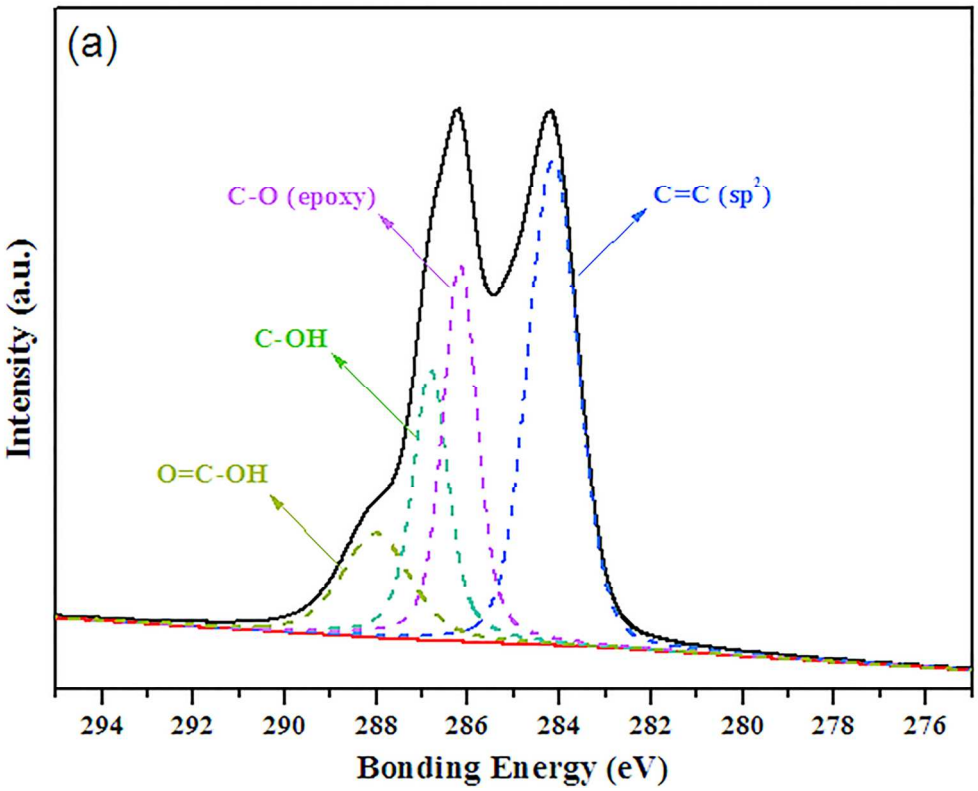

XPS spectra of (a) GO and (b) XGS.
65x52mm (600 x 600 DPI)

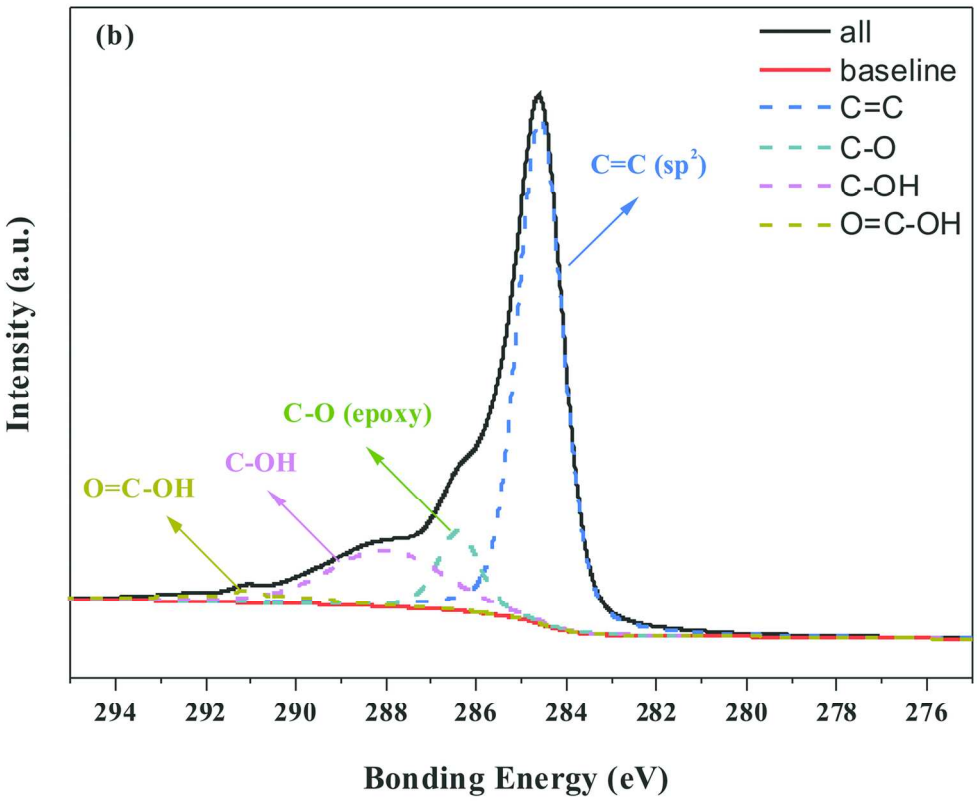

XPS spectra of (a) GO and (b) XGS.
67x54mm (600 x 600 DPI)

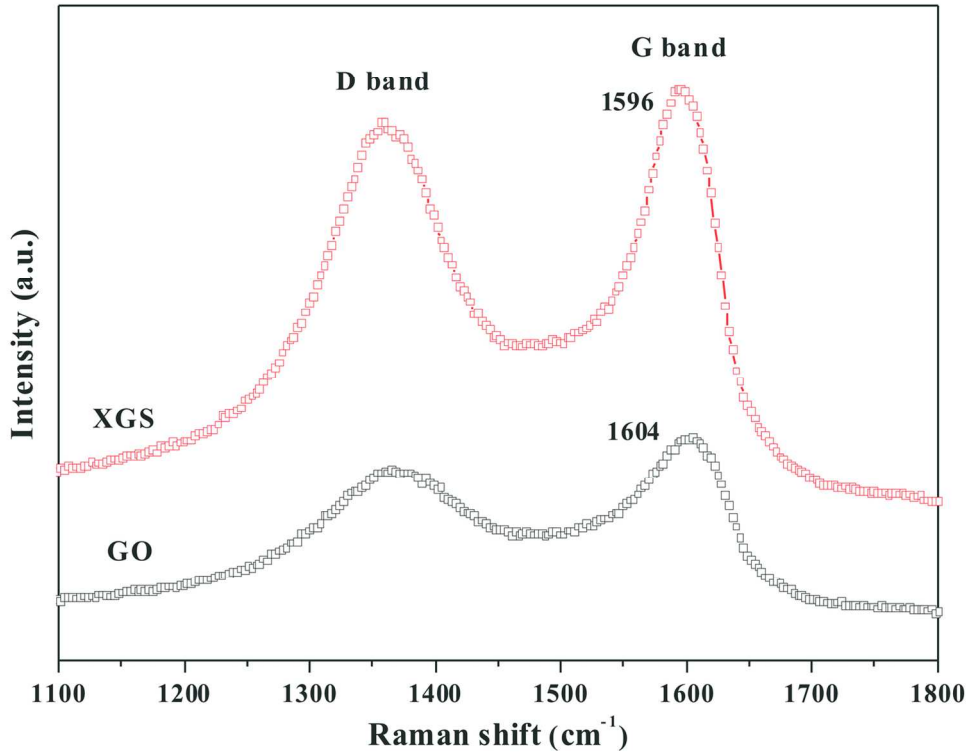

Raman spectra of GO and XGS.
65x52mm (600 x 600 DPI)

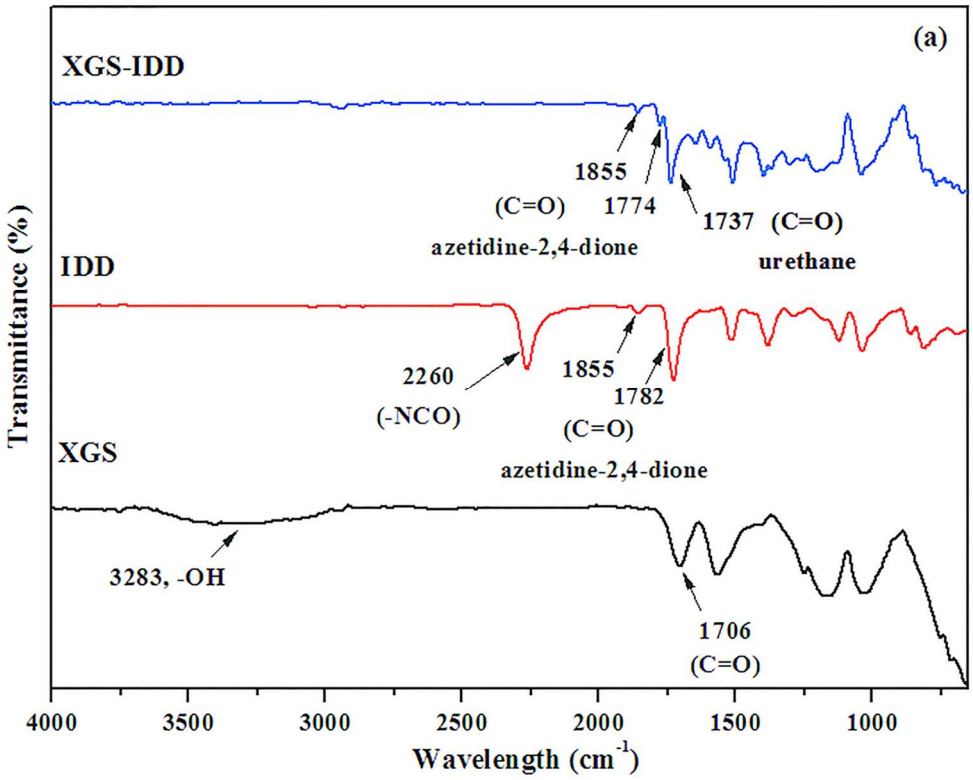

FT-IR spectra of (a) XGS-IDD, (b) XGS-amine, and (c) XGS-G2.5.
64x51mm (600 x 600 DPI)

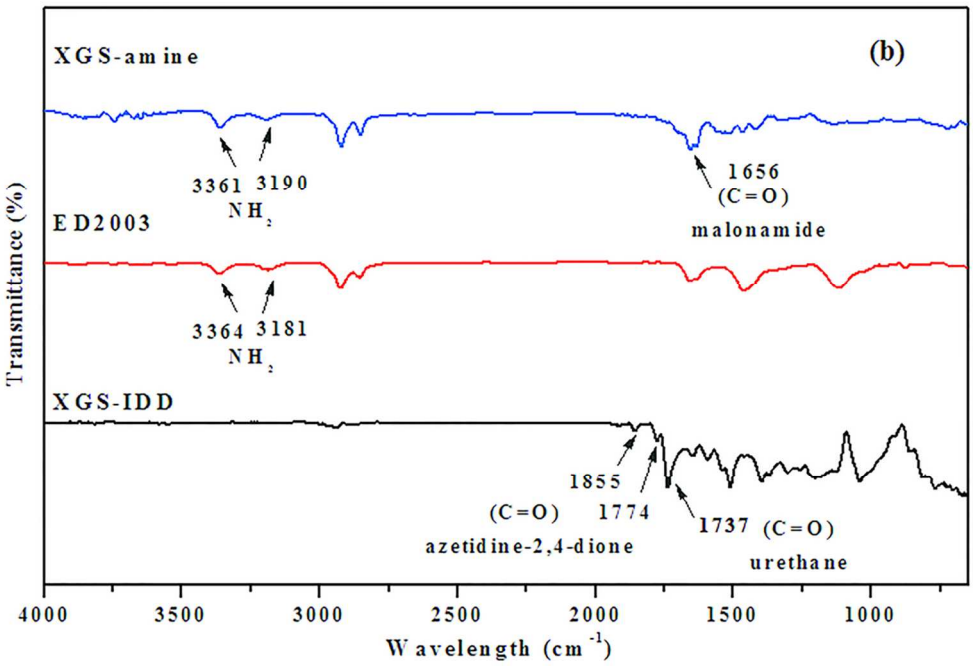

FT-IR spectra of (a) XGS-IDD, (b) XGS-amine, and (c) XGS-G2.5.
55x36mm (600 x 600 DPI)

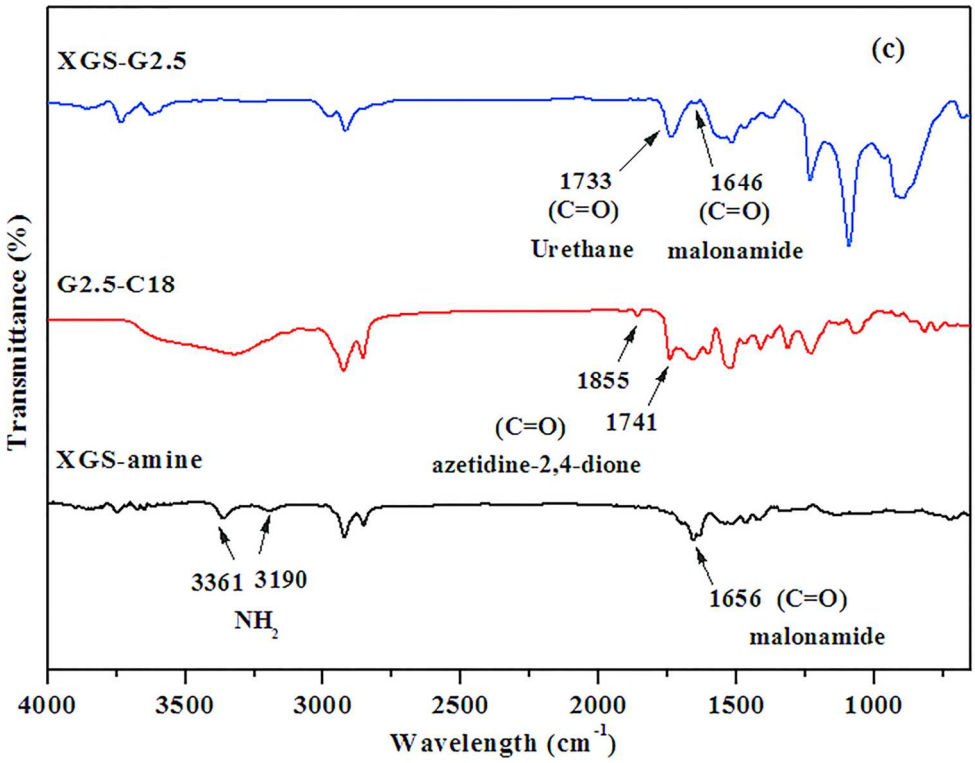

FT-IR spectra of (a) XGS-IDD, (b) XGS-amine, and (c) XGS-G2.5.
63x48mm (600 x 600 DPI)

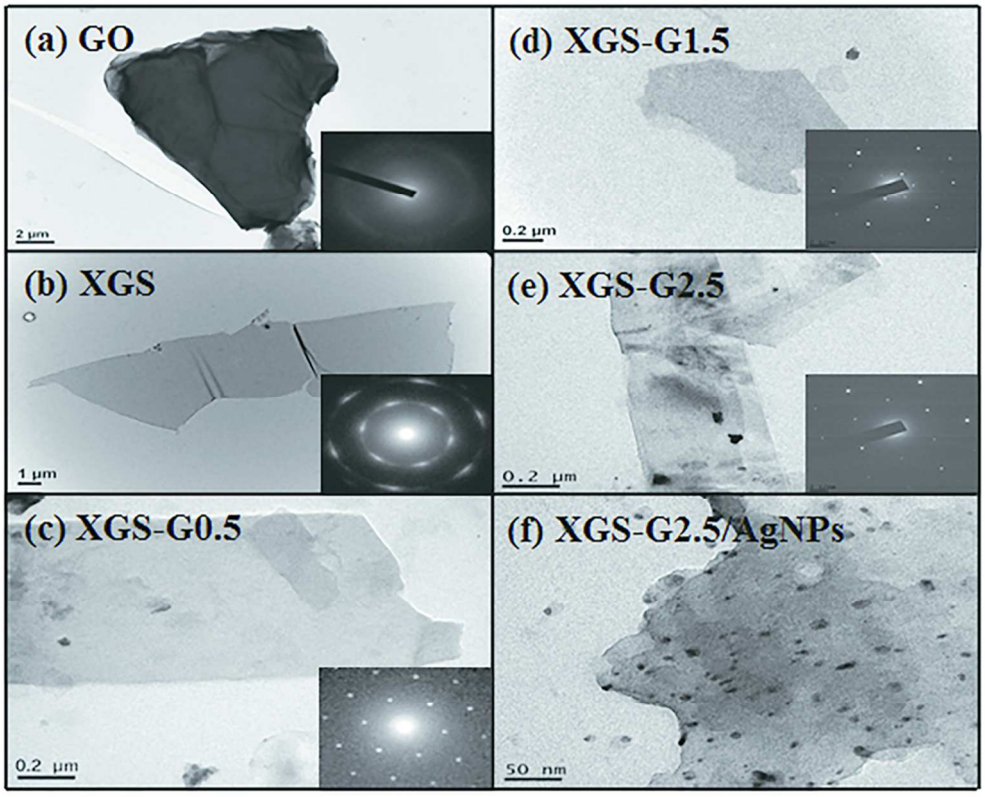

TEM images of GO, XGS, XGS-dendritic derivatives, and XGS-G2.5/AgNPs (Insets show electron diffraction patterns on selected area).
42x34mm (600 x 600 DPI)

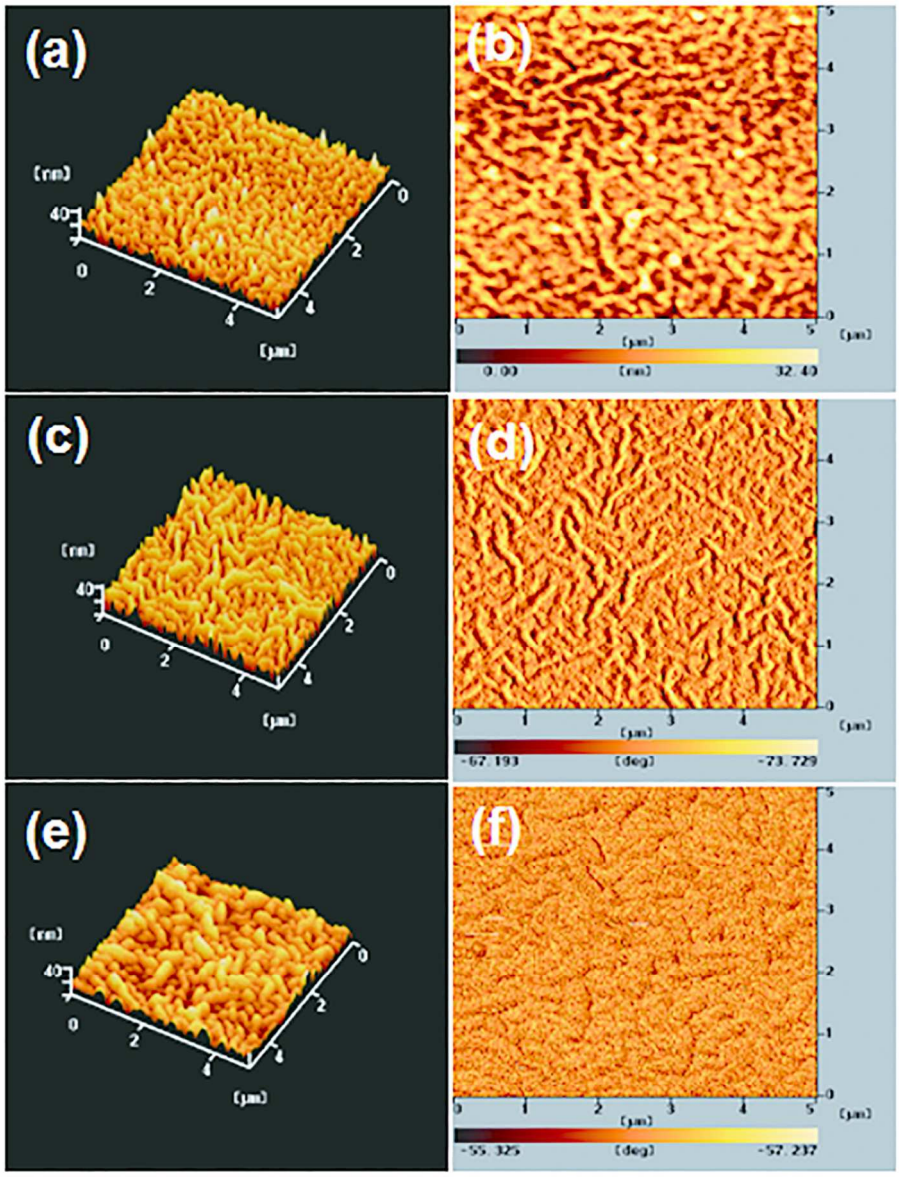

AFM tapping mode (a, c, e,) topographic and (b, d, f) phase images of ZnO (a, b), and PEI/XGS-G2.5 (c, d) and PEI/XGS-G2.5/AgNPs (e, f) coated ZnO films after annealing at 80 °C for 60 min.
68x89mm (600 x 600 DPI)

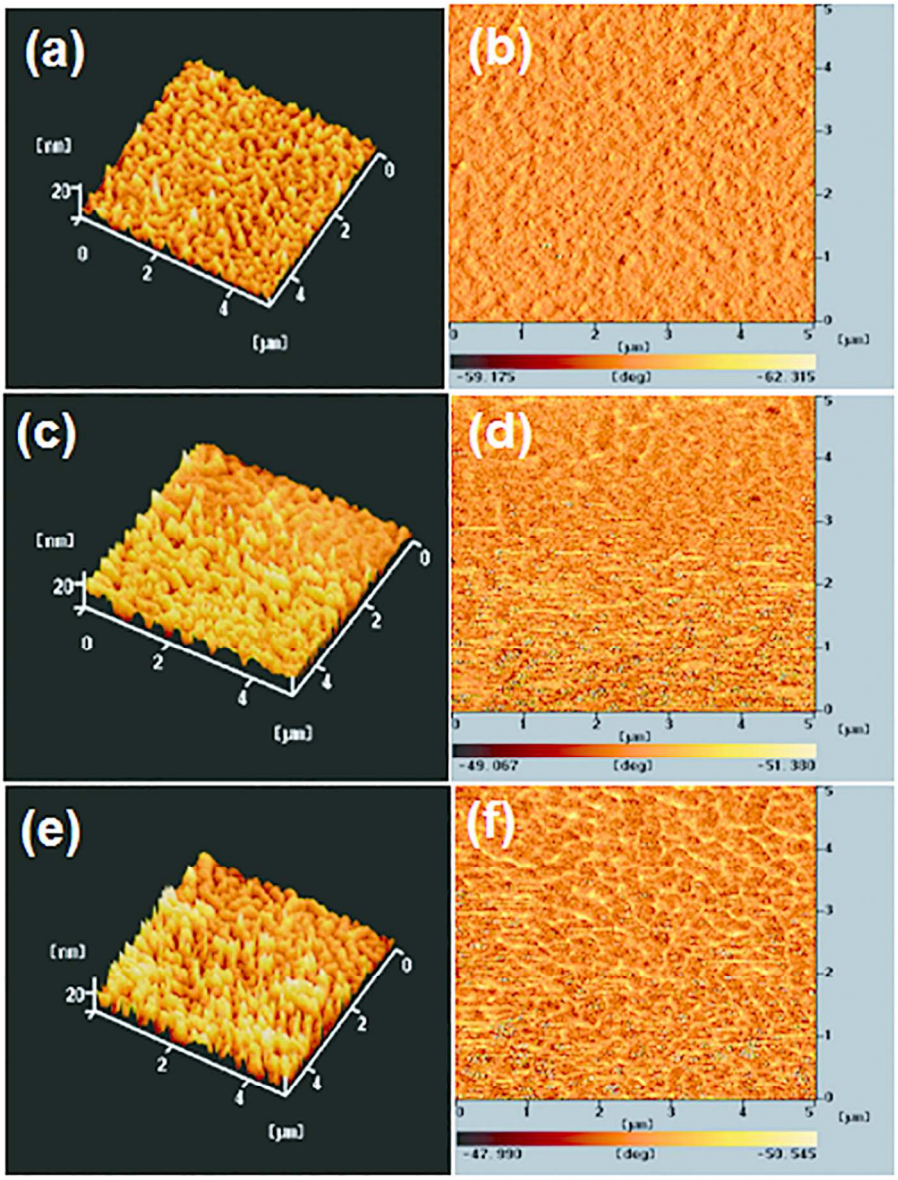

AFM tapping mode (a, c, e,) topographic and (b, d, f) phase images of P3HT:PC61BM layer on the ZnO (a, b), PEI/XGS-G2.5 coated ZnO (c, d), and PEI/XGS-G2.5/AgNPs (e, f) coated ZnO layer annealing at 80 °C for 60 min.
67x87mm (600 x 600 DPI)

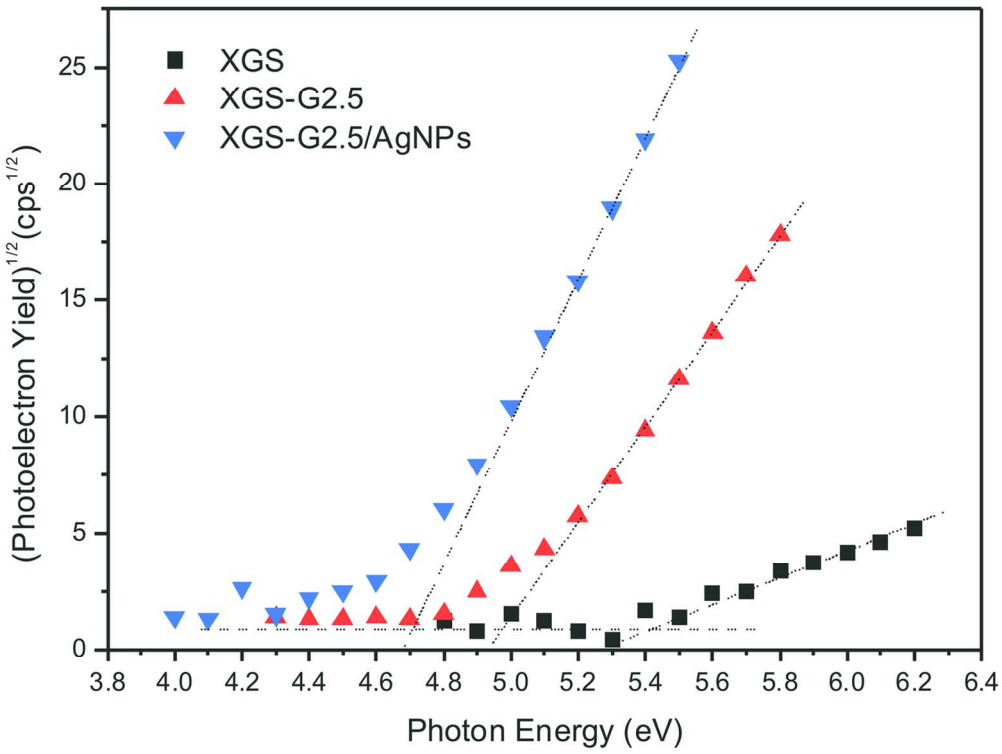

Work functions of XGS, XGS-imine, XGS-G2.5, and XGS-G2.5/AgNPs.
62x47mm (600 x 600 DPI)

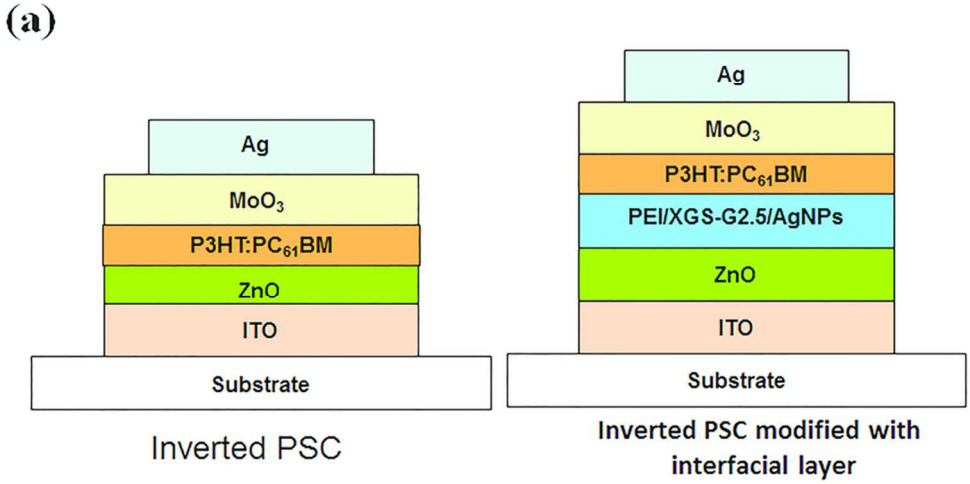

(a) Device architecture of the P3HT/PC61BM-based inverted PSCs using XGS-G2.5/AgNPs as a modifying layer. (b) Schematic illustration on the energy levels of each individual component in the PSCs.
43x23mm (600 x 600 DPI)

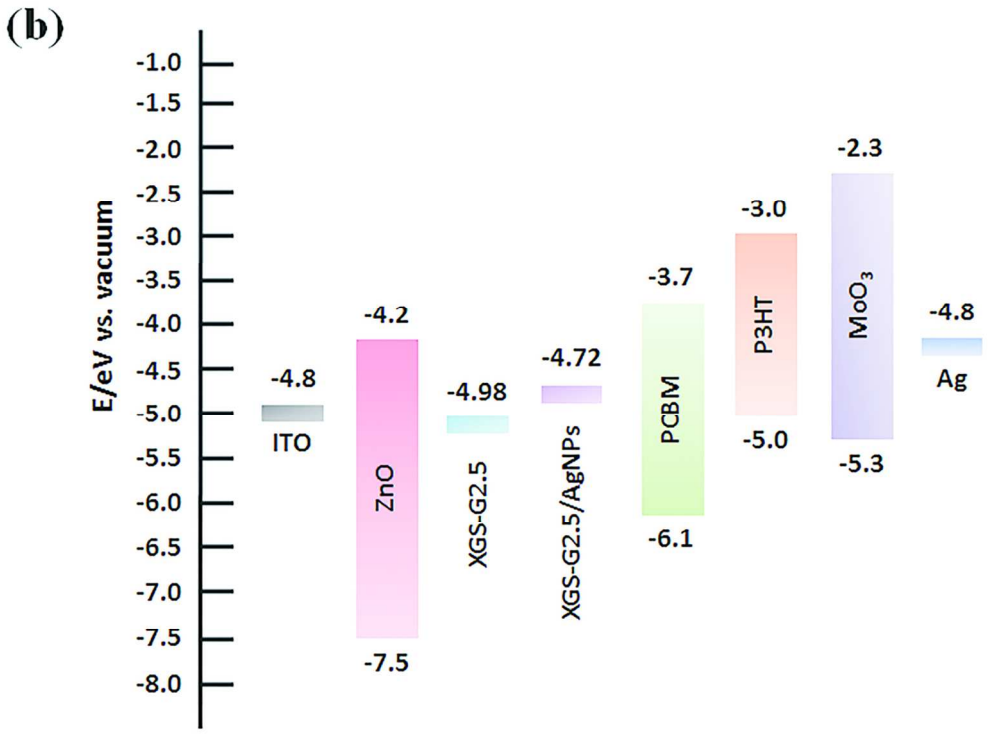

(a) Device architecture of the P3HT/PC61BM-based inverted PSCs using XGS-G2.5/AgNPs as a modifying layer. (b) Schematic illustration on the energy levels of each individual component in the PSCs.
61x46mm (600 x 600 DPI)

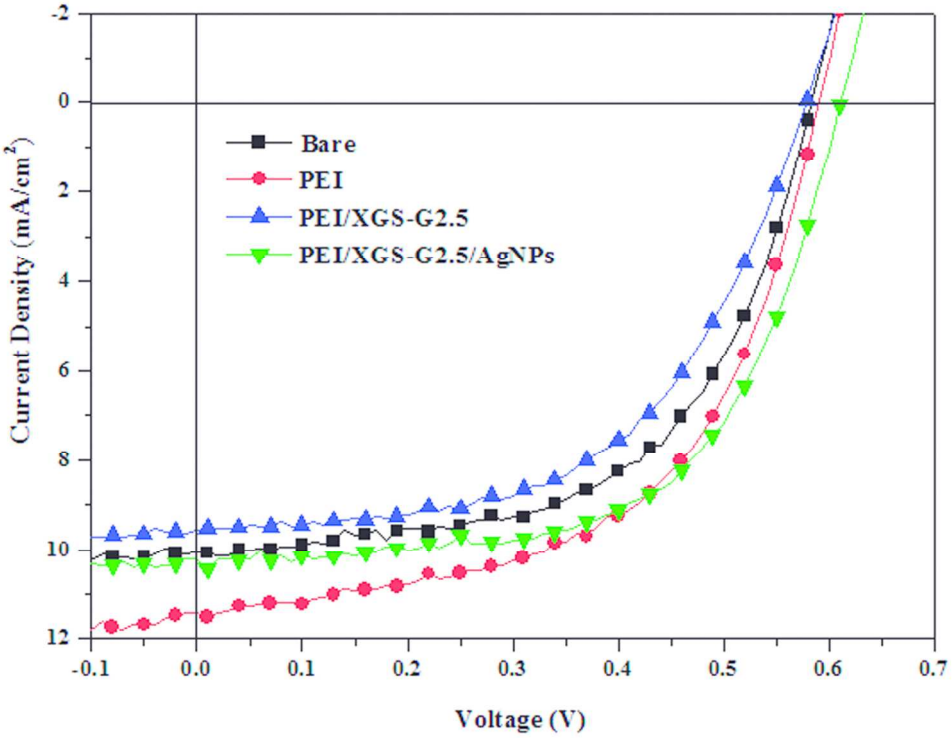

Current density-potential curves of illuminated (AM 1.5G, 100 mW cm-2) P3HT/PC61BM-based inverted PSCs.
64x50mm (600 x 600 DPI)

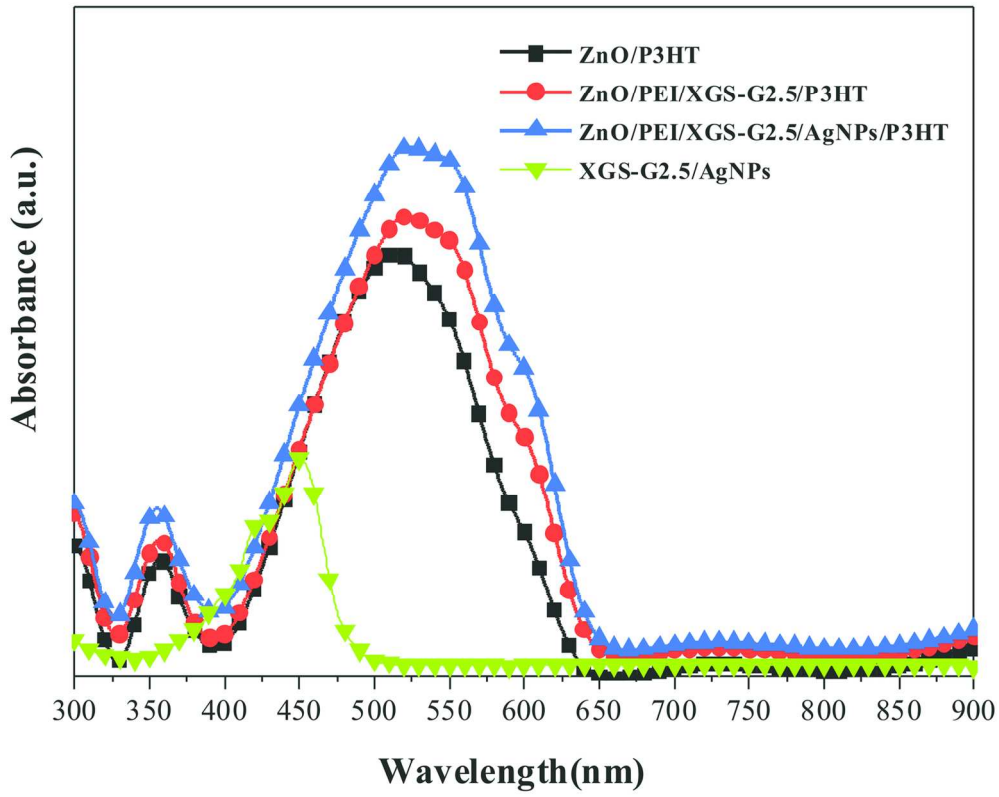

UV-Vis absorption spectra of the P3HT/ZnO, and PEI/XGS-G2.5 and PEI/XGS-G2.5/AgNPs inserted P3HT/ZnO films.
66x53mm (600 x 600 DPI)